On-Line Measurement of Surface Tension and Density with Applications to Emulsion Polymerization

F. J. SCHORK* and W. H. RAY, *Department of Chemical Engineering, University of Wisconsin, Madison, Wisconsin 53706*

Synopsis

Three process sensors are discussed, one for the determination of surface tension and two for the determination of liquid density. All three methods are on-line, compatible with digital data acquisition systems, and capable of monitoring flowing process streams. The instruments are described and calibration data are given. Two mathematical models of the bubble tensiometer are developed. Data showing the application of these instruments to the monitoring of batch and continuous emulsion polymerization are given.

INTRODUCTION

In the past, on-line information about the states of reacting systems was limited, for the most part, to temperature and pressure. With the advent of advanced process control, particularly of digital control, the impetus to determine product quality on-line has increased markedly. In response to this, a number of new sensors have been developed to determine specific process variables continuously. This paper concerns the development of on-line sensors, for the continuous measurement of surface tension and fluid density. These instruments have been used in our laboratory to study the dynamics of emulsion polymerization. Some preliminary experimental results were reported in ref. 1, but the present paper provides the theoretical basis for the instrumentation as well as further experimental data.

Although our prime motivation for the development of the instruments stemmed from our desire to monitor emulsion polymerization reactors, it is clear that these sensors should find application in many other reacting systems where the values of the surface tension and density of the reaction liquid have significance.

ON-LINE MEASUREMENT OF SURFACE TENSION

Surface tension is a difficult property to measure, particularly for systems containing surfactants. Extreme cleanliness and good technique are required to obtain reproducible results. The most widely accepted technique is the Wilhelmy plate procedure which measures the vertical force necessary to balance the force exerted on the plate by the liquid surface as the plate is withdrawn from the liquid. This method is slow and not at all suitable for automated on-line use.

* Present address: School of Chemical Engineering, Georgia Institute of Technology, Atlanta, GA 30332.

Journal of Applied Polymer Science, Vol. 28, 407–430 (1983)
 CCC 0021-8995/83/010407-24$03.40

A new method of surface tension determination has been developed which is continuous, automated, compatible with computer data acquisition systems, and capable of monitoring flowing process streams. This method appears to have widespread applications including monitoring emulsion polymerization. In this section the development of this instrument will be discussed in detail.

Principles of the Bubble Tensiometer

This method is a variant of the well-known maximum bubble pressure technique. A test fluid is introduced into a sample cell in a continuous stream. The liquid level within the cell is maintained by an overflow outlet. Gas bubbles are introduced below the surface of the liquid by two orifices of different diameters. The difference in pressure between the two orifices is sensed continuously and the output signal conditioned to yield a direct measure of the liquid surface tension as shown in Figures 1 and 2.

A relationship between the maximum bubble pressure and the surface tension of a liquid may be obtained as follows. The Schroedinger equation[2] describing a nonspherical bubble may be written as

$$\gamma = \frac{1}{2}P_{\max}r - \frac{1}{3}\rho g r^2 - \frac{1}{2}\rho g r l - \frac{\rho^2 g^2 r^2}{12(P_{\max} - \rho g l)} \tag{1}$$

If eq. (1) is written for each orifice and the equations subtracted, the result may be rearranged to give

$$\gamma = \frac{1}{2}\frac{(P_{1\max} - P_{2\max})}{(1/r_1) - (1/r_2)} - \tfrac{1}{2}\rho g \frac{(l_1 - l_2)}{(1/r_1) - (1/r_2)} + \tfrac{1}{3}\rho g \frac{(r_2 - r_1)}{(1/r_1) - (1/r_2)} + \frac{\rho^2 g^2}{24\gamma}\frac{(r_2^3 - r_1^3)}{(1/r_1) - (1/r_2)} \tag{2}$$

The second term in eq. (2) is a function of the tensiometer dimensions only, and

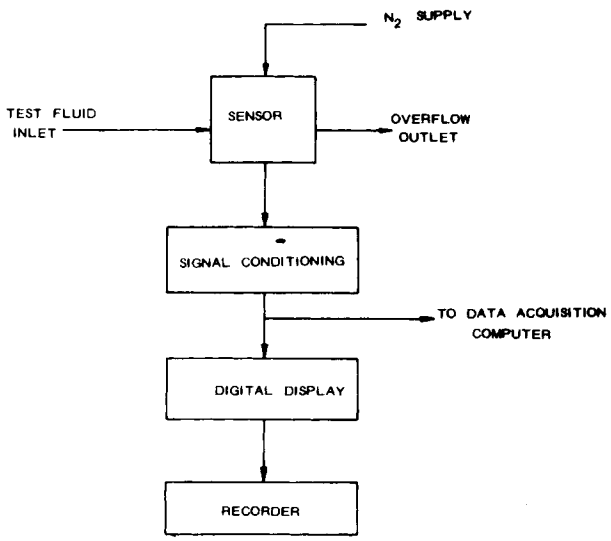

Fig. 1. On-line bubble surface tensiometer schematic.

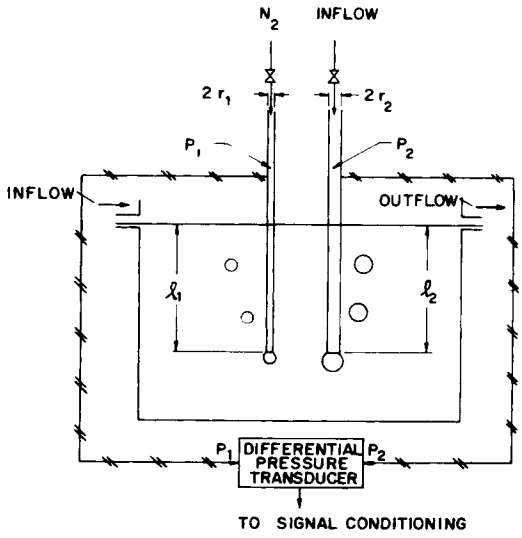

Fig. 2. On-line bubble surface tensiometer detail.

will go to zero if both orifices are at the same depth below the liquid surface. The third and fourth terms are functions of the orifice diameters, fluid density and surface tension. If changes in the last two terms with fluid properties are ignored, they may be lumped together with any difference in orifice depths in a constant denoted as E. Thus a good approximate relationship is

$$\gamma = \frac{1}{2}\frac{(P_{1\max} - P_{2\max})}{(1/r_1) - (1/r_2)} + E \tag{3}$$

which indicates that surface tension is a linear function of the difference in maximum pressures between the two orifices.

Finding the maximum bubble pressure for each orifice and then differencing the maxima requires a rather sophisticated combination of electronic and electromechanical devices. Instead, we have chosen to monitor continuously the difference in pressure by connecting pressure taps from both orifices to the same differential pressure transducer. This signal is then filtered with a low-pass filter to eliminate the transients. The relationship of this measurement to surface tension may be seen from the discussion to follow.

Spherical Bubble Model

The transient behavior of the pressure in each orifice due to the formation and breakage of the bubbles may be understood by referring to Figure 2. The pressure in each orifice may be expressed as a constant term, ρgl, due to the liquid head, plus a periodic function of surface tension. For a large orifice, assuming a spherical bubble, the pressure component due to the surface tension may be written as $2\gamma/b(t)$ where $b(t)$ is the radius of curvature of the developing bubble at time t. The value of $2\gamma/b(t)$ reaches its maximum when $b(t)$ reaches its minimum. At this point, the bubble is hemispheric and $b = r$, the radius of the orifice. As the bubble grows beyond hemispheric, the pressure within the bubble

falls, gas rushes in, and the bubble bursts. The spherical approximation involves significant error for orifices larger than about 0.1 cm. The significance of this approximation will be discussed later in the development of a nonspherical model.

For an orifice at the end of a fine capillary, our visual observations indicate that the mechanism is somewhat different. The liquid is observed to rise up the orifice under the influence of capillary forces to some height h. The equilibrium value of h, h_0 may be calculated as

$$h_0 = 2\gamma \cos \theta / \rho g r_1 \tag{4}$$

Observation of the pressure waveform of the small orifice (via oscilloscope traces of the pressure transducer output) indicates that pressure relaxation between bubbles is not complete, presumably because of the fact that the volume of gas in the total orifice is quite large in comparison with that of a single bubble. Thus there is a minimum pressure P_0 which is not zero. Measurements indicate that the minimum pressure between bubbles is approximately 40% of the maximum bubble pressure, for the small orifice of our current instrument. This bias is included in the following model in the form of a bias factor, $\beta = P_0/P_{\max}$.

If one assumes a capillary rise mechanism for the small orifice, its pressure transient may be written as

$$P_1(t) = \rho g l_1 + \beta \rho g h_0 + \rho g[(1 - \beta)h_0 - h(t)] \tag{5}$$

where $h(t)$ is the height of the capillary column above the orifice tip at any time t. For a constant gas flow rate, this will result in a linear pressure rise with time until the gas–liquid interface reaches the orifice tip and the gas escapes. At the tip there is no change in interface curvature (bubble growth), since the radius of curvature of the interface is already equal to the orifice radius because of the capillary force. If a spherical bubble formation mechanism is assumed for the large orifice, its pressure transient may be written as

$$P_2(t) = \rho g l_2 + 2\gamma / b(t) \tag{6}$$

If the gas flow rates are assumed constant and adjusted to give a specific bubble frequency, $(1 - \beta)h_0 - h(t)$ may be written as

$$(1 - \beta)h_0 - h(t) = \frac{Q_1 t}{\pi {r_1}^2} = \frac{(1 - \beta)(2)\gamma t \cos \theta}{\Upsilon r_1 \rho g} \tag{7}$$

where Q_1 is the volumetric gas flow into the small orifice and Υ is the bubble period. Equation (5) can now be written as

$$P_1(t) = \rho g l_1 + \frac{\beta(2)\gamma \cos \theta}{r_1} + \frac{(1 - \beta)(2)\gamma t \cos \theta}{\Upsilon r_1} \tag{8}$$

For constant gas flow rate, Q_2, the radius of curvature of the bubble on the large orifice is given by:[3]

$$b(t) = \frac{\pi {r_2}^4}{4Q_2 t} + \frac{Q_2 t}{\pi {r_2}^2} \tag{9}$$

Owing to the linearity of the integration operation, subtracting the filtered pressures from the two orifices is equivalent to filtering their difference. Thus it is possible to filter the pressure waveform for each orifice seperately before

differencing them. In addition, if only the pseudo steady value of the filter output is desired, it is not necessary to carry out the rather involved filter integration of the pressure waveform. It may be shown[3] that for a first order filter with time constant τ, and for large t

$$p_f = e^{-t/\tau} \int_0^t p(t')e^{t'/\tau}dt' = \frac{1}{\Upsilon} \int_0^{\Upsilon} p(t)dt \tag{10}$$

If eqs. (6), (8), and (9) are integrated using the pseudo steady form of eq. (10), the filtered waveforms may be written as

$$p_{1_f} = (P_{1_f} - \rho g l_1) = \frac{(1 + \beta)\gamma \cos\theta}{r_1} \tag{11}$$

and

$$p_{2_f} = (P_{2_f} - \rho g l_2) = \frac{3}{2}\frac{\gamma}{r_2} \ln\left(\frac{25}{9}\right) \tag{12}$$

These equations may be subtracted to give the differential filtered pressure ΔP_f:

$$\Delta P_f = \rho g(l_1 - l_2) + \frac{(1 + \beta)\ \gamma \cos\theta}{r_1} - \frac{3}{2}\frac{\gamma}{r_2} \ln\left(\frac{25}{9}\right) \tag{13}$$

For sufficiently large filter time constant, τ, note that ΔP_f is a linear function of surface tension with an intercept equal to the liquid head associated with the difference in depths between the two orifices. In practice, however, the value of the intercept is best found experimentally.

Simulations based on the spherical bubble assumption [eqs. (5), (6), (9), and (11)] were carried out using as parameters the dimensions and operating conditions for the current prototype surface tensiometer as listed in Table I. Simulated and observed waveforms for the large and small orifices and their difference are shown in Figures 3 and 4. As may be seen, the mechanisms discussed above describe adequately the observed pressure transients.

Plotted in Figure 5 are 51 experimental calibration points determined by independently measuring the surface tension of five different test fluids using the Wilhelmy plate method. If one uses regression to determine the constants in eq. (13), one obtains a "universal" calibration consisting of a least squares regression line given by

$$\gamma = 0.060\ (\Delta P_f) + 2.76 \tag{14}$$

with a standard deviation of 1.30 dyn/cm. This may be compared with the "a priori" spherical model [eq. (13)] which uses the bubbler parameters in Table I. However, the quantity $(1 + \beta) \cos\theta$ is unknown. For an assumed value

TABLE I
Tensiometer P1A1 Specifications[a]

$r_1 = 0.052$ cm
$r_2 = 0.362$ cm
$l_1 \simeq l_2 \simeq 2$ cm

[a] Bubble period, both jets: $\Upsilon = 2$ s; filter (first order): $\tau = 60$ s; flow cell volume: $\simeq$20 mL.

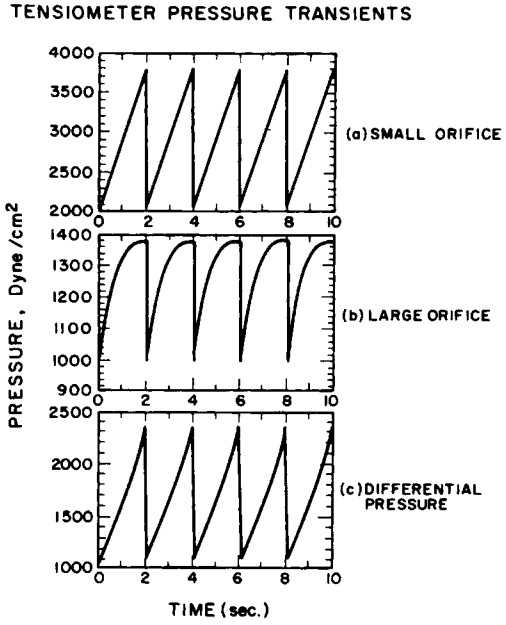

Fig. 3. Simulated pressure transients, bubble surface tensiometer.

$(1 + \beta) \cos \theta = 1.4$ corresponding, for example, to perfect wetting of the glass capillary ($\cos \theta = 1$) and $\beta = 0.4$, the spherical model, eq. (13), becomes

$$\gamma = 0.044 \, (\Delta P_f) \tag{15}$$

As may be seen from curve 1 in Figure 5, there is considerable offset from the

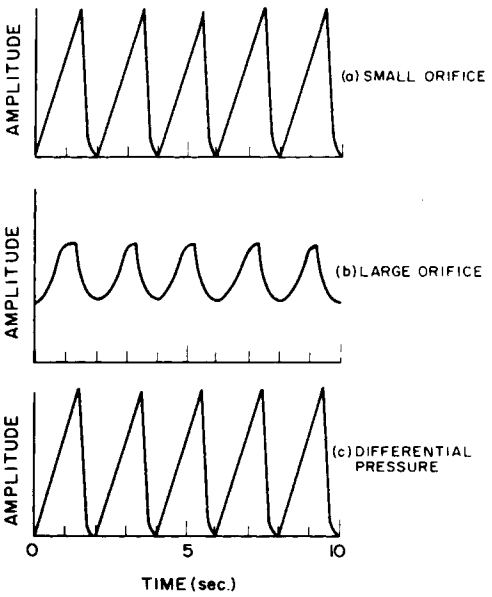

Fig. 4. Measured pressure transients, bubble surface tensiometer.

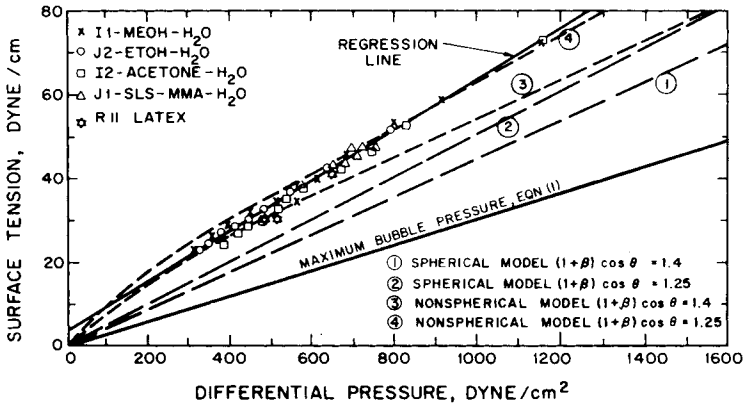

Fig. 5. Calibration curve for bubble tensiometer, prototype P1A1.

experimental regression line, even for the case of some imperfect wetting, such that $(1 + \beta) \cos \theta = 1.25$ (curve 2 in Figure 5). However, the qualitative predictions are in agreement with the regression eq. (14).

The theoretical relationship between γ and $\Delta P_{f,\max}$ for the classical maximum bubble pressure method also is plotted to indicate the differences between the maximum bubble pressure method and the new method reported here. Also shown are the results of a model employing a nonspherical bubble for the large orifice. This will be discussed later.

In order to explore the influence of operating variables on the determination of surface tension with this instrument, a factorial design was carried out using a computer simulation based on the spherical model over three levels of surface tension, two levels of phase lag θ between the two bubbles, and three levels of the ratio of the periods of oscillation, $\Upsilon_1/\Upsilon_2 = R$. The experimental settings and the resulting values of ΔP_f are shown in Table II. A regression analysis indicates that the effects of the three independent variables on the value of ΔP_f may be expressed as

$$\Delta P_f = 632.8 + 996.1S + 1.233F + 2.867R' + 0.486SF + 4.458SR' - 0.280FR' - 0.402SFR' \quad (16)$$

where the independent variables have been scaled as follows to normalize the effect of each variable:

$$S = \frac{\gamma - 28}{72 - 28} \quad (17)$$

$$F = \phi/\pi \quad (18)$$

$$R' = \frac{3\Upsilon}{\Upsilon_1 + \Upsilon_2} - 1 \quad (19)$$

From eq. (16) and Table II it may be seen that the effects of phase lag and frequency ratio on ΔP_f are small, and should not be of major concern in the operation of the instrument. In fact, variation of the phase shift from zero to its maximum at $\theta = \pi$ results in a change of only 0.1% in the value of ΔP_f for distilled water ($\gamma = 72$). Variation of Υ_1/Υ_2 over a factor of 4 results in a change of 0.7% in the value of ΔP_f for distilled water. From the above it may be concluded that

TABLE II
Effect of Operating Conditions on Surface Tension Measurement

Surface tension (dyn/cm)	Phase lag (rad)	τ_1/τ_2	ΔP_f (dyn/cm^2)
72	3.1416	2.0	1637
72	3.1416	1.0	1635
72	3.1416	0.5	1630
72	0.0	2.0	1636
72	0.0	1.0	1633
72	0.0	0.5	1629
50	3.1416	2.0	1137
50	3.1416	1.0	1136
50	3.1416	0.5	1133
50	0.0	2.0	1137
50	0.0	1.0	1133
50	0.0	0.5	1132
30	3.1416	2.0	682
30	3.1416	1.0	682
30	3.1416	0.5	680
30	0.0	2.0	682
30	0.0	1.0	680
30	0.0	0.5	679

the phase lag, which in practice is uncontrollable, will not introduce substantial error into the measurement of surface tension. The frequencies of bubbling, hence the periods for the orifices, are easily controlled by adjusting the gas flow rates when calibrating the instrument. This should be done to prevent unnecessary error in the measurement. Once set, the frequencies will not vary enough because of changes in surface tensions to bias the measurement substantially. Thus for most applications, the gas flow rates need not be reset for each test liquid.

Nonspherical Bubble Model

The model and instrument calibration discussed thus far both assume that the bubble attached to the large orifice is a spherical cap, is at all times a spherical section, and detaches from the orifice when its shape becomes hemispheric. In practice, for orifices having radii greater than 0.1 cm, this is a poor approximation because the gas and liquid phases have different densities resulting in a buoyancy force on the bubble which distorts its shape into something roughly approximated by an elipse. In this section, then, we shall use a more detailed, nonspherical bubble model to analyze the performance of the bubble tensiometer.

The actual geometry of bubbles from the large orifice is shown in Figures 6 and 7. Since there is no single radius of curvature for the nonspherical bubble, it is not possible to predict, based on the geometry alone, at what point in its growth the bubble will burst. To study the development of the nonspherical bubble, then, it is necessary to resort to an elementary force balance across the interface, reduce this to a second order differential equation in two space variables, and then solve this equation numerically.

The true shape of a bubble may be developed from the fundamental equation of a curved surface. Referring to Figure 6, the pressure inside the bubble (less the hydrostatic pressure, ρgl) may be written as

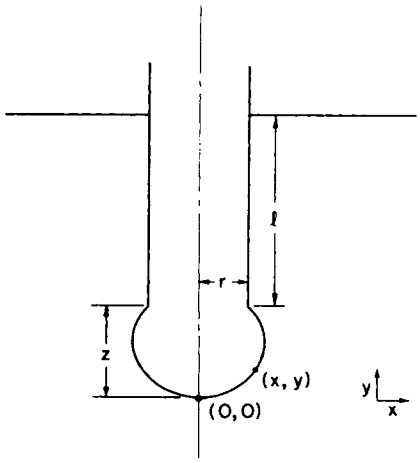

Fig. 6. Nonspherical bubble.

$$p_{\text{int}} = \gamma(1/R_1 + 1/R_2) + \rho g(z - y) \tag{20}$$

where R_1 and R_2 are the principal radii of curvature of the interface at any point (x,y). This is known as the Young–Laplace equation.[2] Since the pressure inside the bubble is the same at all points on the interior, p_{int} may be calculated at the point (0,0) as

$$p_{\text{int}} = 2\gamma/b + \rho g z - 0 \tag{21}$$

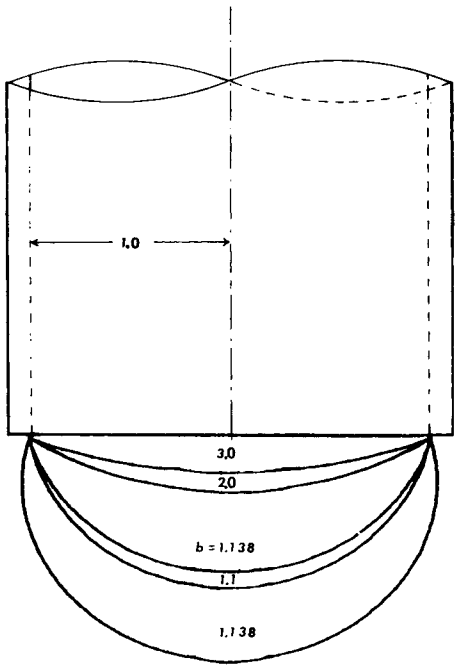

Fig. 7. Nonspherical bubble profiles calculated from the fundamental equation of an interface, $r = 0.20$ cm, $\rho = 1.0$ g/cm^3, $\gamma = 72$ dyn/cm.

At this point, owing to symmetry considerations, the two principal radii of curvature are equal and denoted by b. If the values of p_{int} in eqs. (20) and (21) are set equal, the fundamental equation of the bubble interface results:

$$\gamma(1/R_1 + 1/R_2) = 2\gamma/b + \rho g y \tag{22}$$

Since the profile of a bubble is a figure of revolution, the principal radii at (x,y) can be written, from geometric considerations[2] as

$$\frac{1}{R_1} = \frac{d^2y/dx^2}{[1 + (dy/dx)^2]^{3/2}} \tag{23}$$

$$\frac{1}{R_2} = \frac{(1/x)\, dy/dx}{[1 + (dy/dx)^2]^{1/2}} \tag{24}$$

Equations (23) and (24) may be substituted into eq. (18) and the result rearranged to give

$$\frac{d^2y}{dx^2} = -\frac{1}{x}\frac{dy}{dx}\left(1 + \left(\frac{dy}{dx}\right)^2\right) + \left(\frac{2}{b} + \frac{\rho g r^2}{\gamma} y\right)\left(1 + \left(\frac{dy}{dx}\right)^2\right)^{3/2} \tag{25}$$

The bubble can then be normalized with respect to r, the radius of the orifice, by the following change of variables:

$$x' = x/r \tag{26}$$

$$y' = y/r \tag{27}$$

$$b' = b/r \tag{28}$$

Thus the present scaling (with respect to r) is simpler than scaling with $b(t)$ as was done in the more general formulation.[4] Hence the scaling parameter does not vary with time as the bubble develops. Defining

$$\zeta = 2/b' \tag{29}$$

and

$$\eta = \frac{\rho g r^2}{\gamma} \tag{30}$$

eq. (25) becomes

$$\frac{d^2y'}{dx'^2} = -\frac{1}{x'}\frac{dy'}{dx'}\left(1 + \left(\frac{dy'}{dx'}\right)^2\right) + (\zeta + \eta y')\left(1 + \frac{dy'}{dx'}\right)^{3/2} \tag{31}$$

The boundary conditions are known from the geometry:

$$x' = 0, \quad y' = 0, \quad dy'/dx' = 0 \tag{32}$$

Equation (31), then, is the fundamental equation of the bubble interface, and as such defines the profile of the bubble. The constant ζ is a function of the bubble size (through b) and varies as the bubble grows. The constant η, however, is a function only of the properties of the system and defines the shape of the bubble as well as its development with time. Equation (31) is written for a bubble blown downward into a liquid. The same equation with the sign of η reversed applies for a bubble being blown upward into a liquid or, with a different scaling, applies as well to the hanging or sesile drop of liquid in a gas.

Equation (31) was solved numerically using the Episode package for systems

of stiff ordinary differential equations to yield the profiles of bubbles formed from orifices of given dimensions into a liquid of specified properties. The development of a bubble was studied by tracing bubble profiles for various values of b. A set of profiles showing the development of the bubble with time (changing b) solved by this method is shown in Figure 7. Inspection of this figure indicates that as the bubble grows, the value of b goes from ∞ at $t = 0$, through a minimum as the bubble forms, then increases again as the widest point of the bubble extends beyond the radius of the orifice. Since, unlike the spherical bubble there are now two terms associated with pressure development [as shown in eq. (20)], the point of burst is not determined by the value of b alone, but by the point at which the pressure within the bubble stops rising with additional volume. Thus the bubble bursts at the point at which $dp/dV = 0$. To determine this burst point in our simulation, the value of p was calculated for each completed profile from eq. (21), and V was calculated by numerically integrating across the bubble profile.

Using the solution scheme outlined above, the pressure–volume relationships during development of bubbles under a variety of conditions have been studied. These are plotted as $P - \rho gl$ in Figures 8 and 9 so that the capillary depth terms are not a factor. Figure 8 shows the effect of surface tension on the pressure–volume curve for an orifice of 0.362 cm radius. The bubble volume has been scaled by the volume of a hemispheric bubble with a radius equal to that of the orifice. Thus the comparable curves for the spherical bubble stop at $V = 1$. For both bubble models, the pressure rise is a strong function of the surface tension and bursting occurs at the point of instability ($dp/dV = 0$.) The location of this point has been noted on the curve. Figure 9 shows that the density of the liquid has an increasing effect on the evolution of the pressure–volume curve as the bubble becomes larger in size. This effect is neglected for the spherical bubble approximation.

The fact that the pressure evolution is significantly influenced by the density led us to try to develop a mathematical model for the bubble tensiometer that would include the effects of nonsphericity. Such a model could then be used to improve the accuracy of the instrument. Because no analytical solution to the fundamental equation [eq. (31)] exists, it was decided to develop an ap-

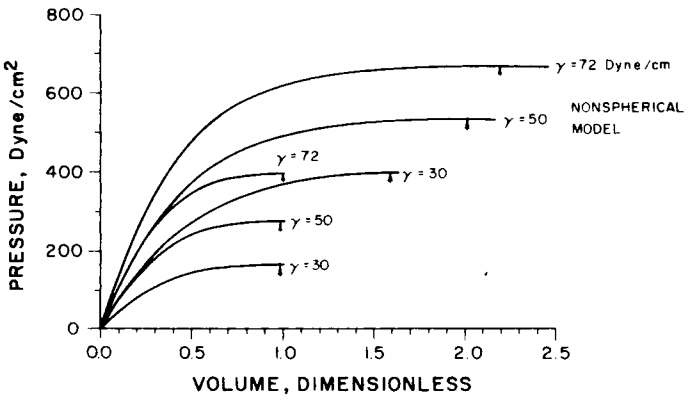

Fig. 8. Spherical and nonspherical bubble pressure development as a function of surface tension. $\rho = 1.0$ g/cm^3; $r = 0.362$ cm; arrow indicates maximum.

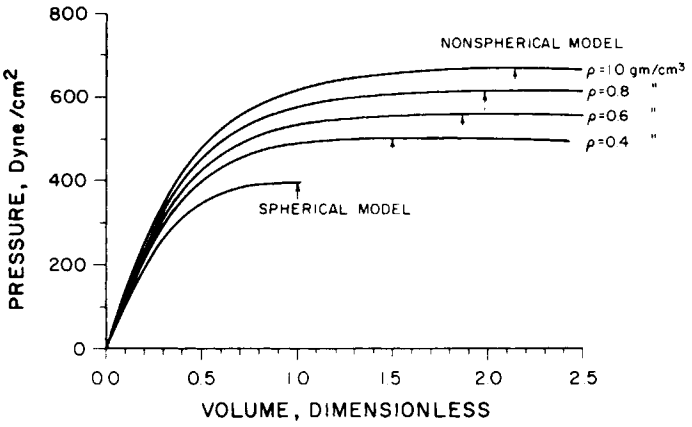

Fig. 9. Spherical and nonspherical bubble development as a function of density. $\gamma = 72$ dyn/cm; $r = 0.362$ cm; arrow indicates maximum.

proximate operating equation that retains the structure of the problem while allowing the coefficients to be determined by regression against calibration data.

Inspection of Figures 8 and 9 indicates that the pressure development might be approximated by a first order rise to the maximum bubble pressure. The maximum pressure is well represented by eq. (1) for high γ values, but is more accurately determined from simulations for low values of γ. Using $p_{\max} = 2\gamma/r$ in the last term, eq. (1) becomes

$$p_{2_{\max}} = \frac{2\gamma}{r_2} + \frac{2}{3}\rho g r_2 + \frac{\rho^2 g^2 r_2^3}{12\gamma} \tag{33}$$

The pressure development shown in Figures 8 and 9 may then be approximated by

$$p_2(t) = p_{2_{\max}}\left[1 - \exp\left(-\frac{V}{\tau_1 V_{\max}}\right)\right] = p_{2_{\max}}\left[1 - \exp\left(-\frac{t}{\Upsilon\tau_1}\right)\right] \tag{34}$$

The validity of the first order rise approximation may be investigated by reference to Figure 10 where

$$\ln\left(\frac{p_{\max} - p(t)}{p_{\max}}\right)$$

is plotted against $V/V_{\max}$ for data generated by numerical solution of the fundamental equation for various values of $\eta = \rho g r^2$. For a first order system, such a plot should result in a series of straight lines. As may be seen, the curves may indeed be approximated by straight lines. It will be noticed that for various values of η the slopes of the lines differ, indicating differing values of the time constant, τ_1, of the first order rise. If the slope for each value of η is evaluated by regression of the data, and the resulting values of $\tau_1(\tau_1 = 1/\text{slope})$ are plotted versus η, the result is an approximately quadratic relationship. Regression of τ_1 against η results in the following relationship:

$$\tau_1 = (4.2 + 2.335\eta - 0.738\eta^2)^{-1} \tag{35}$$

The above discussion results in the approximation of any of the pressure–

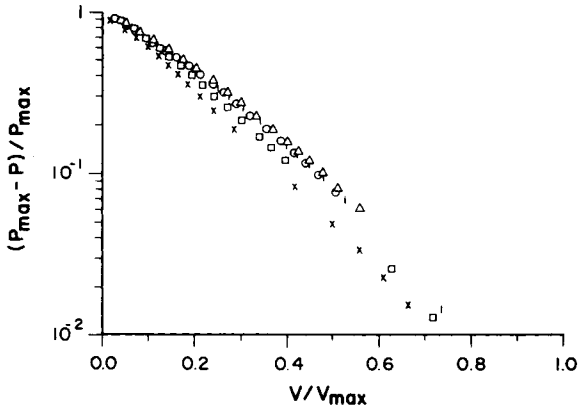

Fig. 10. First order approximation to bubble pressure rise. ○, $\eta = 0.436$; □, $\eta = 0.490$; △, $\eta = 0.545$; ×, $\eta = 0.785$; 1, $\eta = 1.31$.

volume curves in Figures 8 and 9 by a first order rise to p_{max} as shown in Figure 11. Approximations for other pressure–volume curves are of about the same accuracy. Note that this approximation to the nonspherical behavior is much better than the spherical bubble approximation also shown on Figure 11. Putting eq. (34) into eq. (10), the filtered pressure becomes

$$p_{2f} = p_{max}(1 - \tau_1 + \tau_1 e^{-1/\tau_1}) \tag{36}$$

where p_{max} is determined as discussed above.

A model employing a capillary rise for the small orifice [eq. (11)] and a first order rise to the maximum pressure for the large orifice [eq. (34)] can be written as follows:

$$\Delta P_f = \frac{(1+\beta)\gamma \cos\theta}{r_1} - (1 - \tau_1 + \tau_1 e^{-1/\tau_1})p_{max} \tag{37}$$

It is possible to use this theoretical model for the nonspherical bubble (together with the tensiometer parameters in Table I) to provide an *a priori* prediction of the 51 data points shown in Figure 5. Unfortunately, density data are not

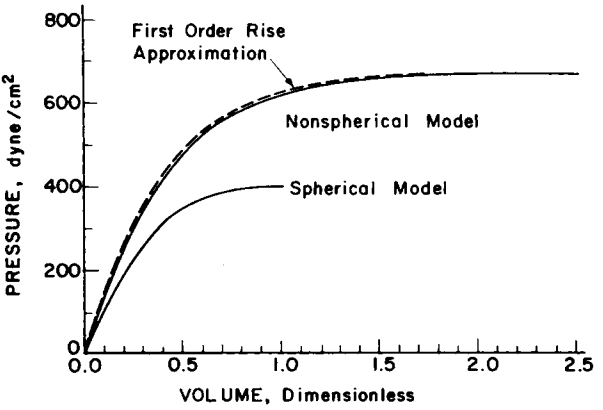

Fig. 11. Comparison of spherical model, nonspherical model, and first order rise approximation for bubble pressure development, $\eta = 1.785$.

available for these so $\rho = 1$ was chosen in each case. Because the factor $(1 + \beta)$ $\cos \theta$ is not known exactly, two plausible values are selected: 1.40 (curve 3) and 1.25 (curve 4). Note that the completely theoretical model (curves 3 or 4) even without including density variations, does a much better job than the spherical bubble model in predicting the γ vs ΔP_f relationship.

Although a simple linear regression in the form of eq. (14) correlates the data very well, it is a useful question whether a regression expression using the nonspherical bubble model might do better. By using eq. (33) for $p_{2\max}$ with the approximation

$$\gamma = \frac{1}{2} \Delta P_f \left(\frac{1}{r_1} - \frac{1}{r_2} \right)$$

in the last term, eq. (37) provides an equation suitable for regression in the form

$$\gamma = B_1 \Delta P_f + B_2 \psi \rho + B_3 \psi \rho^2 / \Delta P_f \tag{38}$$

where

$$\psi = (1 - \tau_1 + \tau_1 e^{-1/\tau_1}) \tag{39}$$

By using 28 calibration points where surface tensions were independently determined and density measurements were from the DMA40 densitometer, one obtains the following least squares regression expression

$$\gamma = 0.0664\ \Delta P_f - 9.582\ \psi \rho + 5053\ \psi \rho_2 / \Delta P_f \tag{40}$$

The sample standard deviation in γ for this regression is $\sigma_\gamma = 1.34$ dyn/cm. This may be compared with *regression* using the functional form of the spherical model [eq. (13)] on the same 28 data points yielding

$$\gamma = 0.064\ \Delta P_f \tag{41}$$

with sample standard deviation, $\sigma_\gamma = 1.70$ dyn/cm. Thus the nonspherical model provides a better functional form for regression than the spherical model. However, as noted above, an empirical form such as eq. (14) seems to do just as well in correlating this limited number of data points. It is felt, however, that the bulk of the residual error results from measurement error in both the Wilhelmy plate standards and in the present form of the tensiometer, and not from the lack of fit of the model. Thus, the nonspherical model, when used to correlate more precise data over a wider density range, should produce improvements in the accuracy of the instrument.

Bubble Tensiometer with Density Correction

A second design for the surface tensiometer that should result in increased accuracy has been developed. It will be recalled that if the nonspherical model of eq. (37) is used, the surface tension measurement is corrected for variations in the liquid density. The terms containing density, however, cannot be included in the operating equation of the instrument described previously since the fluid density is unknown. If an additional orifice is placed in the sample cell with a depth greater than that of the other orifices and a radius equal to that of the larger orifice, an independent determination of fluid density can be made by measuring

the differential pressure between the new, deep orifice and the original large orifice. Since the two orifices have the same radii, the differential signal contains no surface tension component. Because the two orifices are at different depths, the differential signal will be proportional to fluid density. It is also possible, of course, to use four orifices, two each for surface tension and density. Details of the measurement of density by this technique are given in the next section.

Once the density is known, eq. (37) may be used to calculate the surface tension based on the measured density and differential pressure. The use of this equation should significantly reduce the instrument error, since the effect of fluid density has been accounted for.

ON-LINE MEASUREMENT OF DENSITY

Two methods of liquid density determination have been used, based on two entirely different approaches. The first, and most successful at this time, is based on the DMA-series digital densitometer. This method is adequately discussed in refs. 1 and 3, and will not be discussed here. A second method is based on hydrostatic head as sensed through the back pressure from two orifices at different submersion depths. This method may be used as an independent measure of liquid density, but it will also likely be used in conjunction with the bubble tensiometer as a density correction to the surface tension measurement.

Bubble Densitometer

During the development of the bubble tensiometer, it was decided to use the same technique to measure density on-line. An instrument based on this technique would offer more flexibility in mounting and less vulnerability to fouling than the Mettler densitometer, and could be incorporated into the same housing as the bubble tensiometer.

The densitometer involves the use of two submerged orifices, but unlike the tensiometer, the orifices are of equal radii and mounted at unequal depths. (See Fig. 12). In addition, the orifice radii are chosen sufficiently large to have negligible capillary forces. If this measurement were integrated with the tensiometer, only three orifices would be necessary, since the large orifice of the tensiometer would serve as one of the two legs of the densitometer. In the prototype, two orifices of 0.218 cm radius are mounted in a flow cell similar to the one for the tensiometer. The orifices are mounted so that the difference in depth between them is 1.9 cm. A sensitive differential pressure transducer is connected to pressure taps from the two orifices. Compressed gas is bubbled through both orifices at the rate of about one bubble every 2 s, although the gas flow rate is not critical. As in the tensiometer, the pressure necessary to form each bubble is the sum of the pressure due to the liquid head and the pressure necessary to generate new interfacial surface (the surface tension effect). In the case of the tensiometer, the head terms cancel when one measures differential pressure since the orifices are at equal depths. In the case of the densitometer, the surface tension terms cancel since the two orifices are of the same radius and the difference in head is measured. This is, of course, just the density multiplied by the difference in depths and the gravitational constant. Thus the filtered differential pressure is a linear function of density. Integrating this measurement

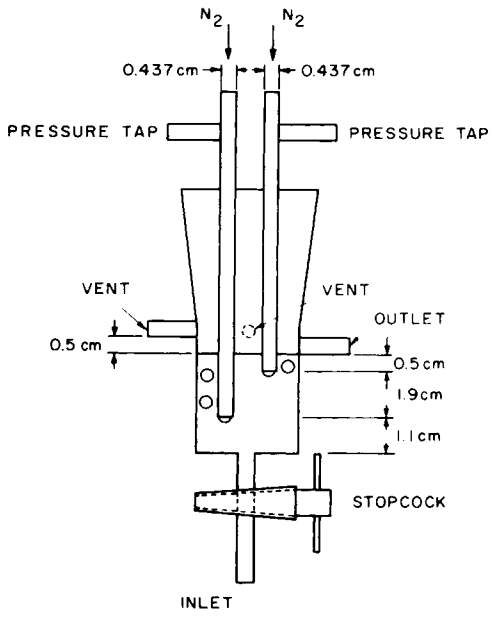

Fig. 12. Prototype bubble densitometer.

with the tensiometer would require an additional orifice, pressure transducer, and filter.

Figure 13 shows the results of a calibration for our prototype using 31 samples of various densities. The densities were determined independently using the Mettler DMA40 densitometer. The standard deviation about the regression line is $\pm 5.9 \times 10^{-3}$. Thus we can measure six parts per 1000 or 0.6%. While this should be sufficient for many applications, some applications would require density to be known with greater precision. For example, for use as a measure of monomer conversion in emulsion polymerization, this prototype measures conversion with a standard deviation of about 6%. While few instruments are available for on-line use which can give even this precision, efforts aimed at improving the resolution would be well spent.

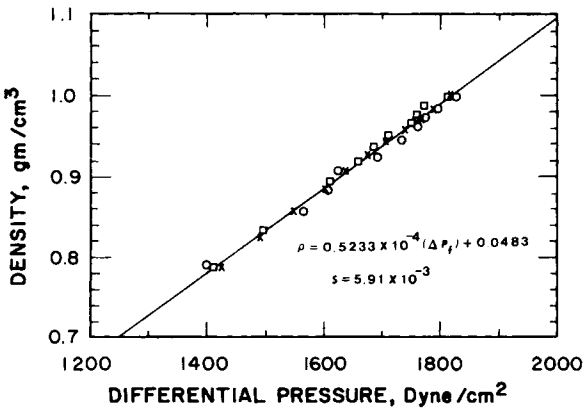

Fig. 13. Bubble densitometer calibration, prototype D1A1. $\rho = 0.5233 \times 10^{-4}\ (\Delta P_f) + 0.0483$; $s = 5.91 \times 10^{-3}$.

Although the resolution of this bubble densitometer is not as good as that of some off-line methods, it offers the same advantages as the tensiometer in terms of durability and continuous on-line measurement. In addition, the densitometer can be integrated with the tensiometer to provide two sensors in one installation.

APPLICATIONS

The sensors described above have been used to monitor both batch and continuous emulsion polymerizations of methyl methacrylate. The flowsheet for the bench-scale reactor system is shown in Figure 14. During both batch and continuous polymerizations a small stream of emulsion is continuously pumped from the reactor and through the sensors. In all the experiments the emulsifier was sodium lauryl sulfate (SLS) and the initiator was ammonium persulfate. Before presenting preliminary data showing the utility of these sensors, it will be necessary to discuss the relationship between surface tension and free emulsifier concentration.

Free Emulsifier Concentration

Although it is the surface tension of the latex which is measured, it is the free emulsifier concentration which is critical to the reaction dynamics. Recall that in emulsion polymerization, as the polymer particles grow with increasing conversion, the free emulsifier concentration falls because of additional surfactant being adsorbed onto the new polymer surface. As the free emulsifier concentration falls, the surface tension of the aqueous phase rises above the value at the critical micelle concentration (CMC). The free emulsifier concentration may be determined directly from the surface tension by reference to Figure 15. Plotted are surface tensions (as determined by the Wilhelmy plate method) of solutions of sodium lauryl sulfate (the polymerization emulsifier) in water. Curve A shows the results for pure water; curve B shows the results for water saturated

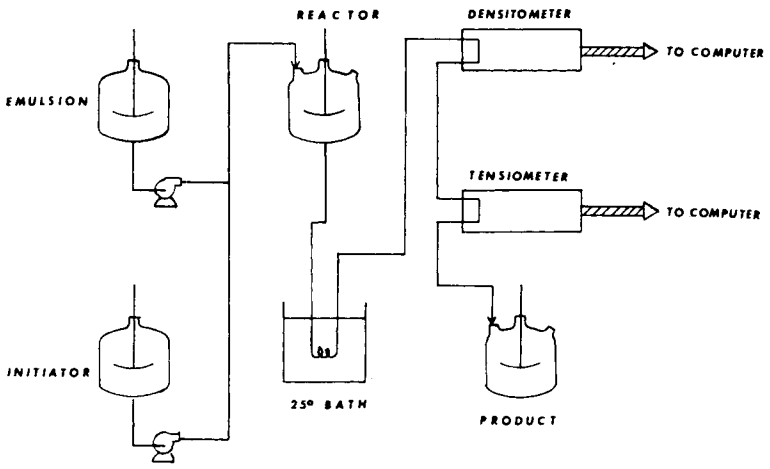

Fig. 14. Continuous polymerization flowsheet.

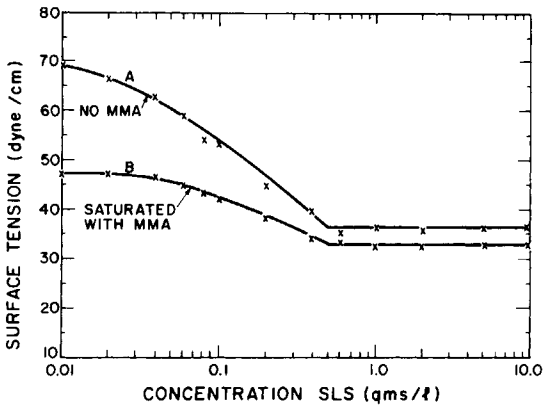

Fig. 15. Wilhelmy plate measurements of surface tension for SLS solutions: A, no MMA; B, saturated with MMA.

(1.4 wt %) with methyl methacrylate. Since the methyl methacrylate concentration did not exceed its solubility in water, no monomer droplets were present. As may be seen from the graph, the presence of methyl methacrylate has a relatively small effect on the critical micelle concentration or on the surface tension at the critical micelle concentration. This is due to the fact that methyl methacrylate is only slightly surface active, and its effect is far overshadowed by that of the sodium lauryl sulfate. At low surfactant concentrations, however, the effect of the methyl methacrylate becomes significant, and the surface tension in the presence of methyl methacrylate is much lower than in its absence. By making use of curves such as those in Figure 15, one may relate measured surface tension to free emulsifier concentration for any emulsion polymerization. When the free emulsifier concentration rises above the CMC, it is necessary to use titration back to the CMC (while monitoring with the tensiometer) to determine the free emulsifier concentration.

Emulsion Polymerization Monitoring

Examples of the application of on-line determination of surface tension and density to emulsion polymerization are detailed in this section. Conversion and surface tension were monitored by continuously removing a stream of emulsion from the reactor and passing it through the densitometer and tensiometer. Total sampling delay from the reactor to the sensors was less than 8% of one reactor residence time. An example of the monitoring of a batch emulsion polymerization of methyl methacrylate is shown in Figure 16. Monomer conversion based on density measurement with the digital densitometer, and values of conversion determined off-line by the traditional gravimetric method are shown. As may be seen, the two methods agree quite well, and in fact, the largest error can probably be attributed to inaccuracies in sampling and analysis for the manual method. Also shown in Figure 16 is the surface tension of the emulsion as a function of time during the same polymerization. Note that the surface tension is initially at its critical micelle concentration value, indicating the presence of micelles. Note also that the surface tension rises away from the critical micelle concentration very early in the polymerization, indicating the

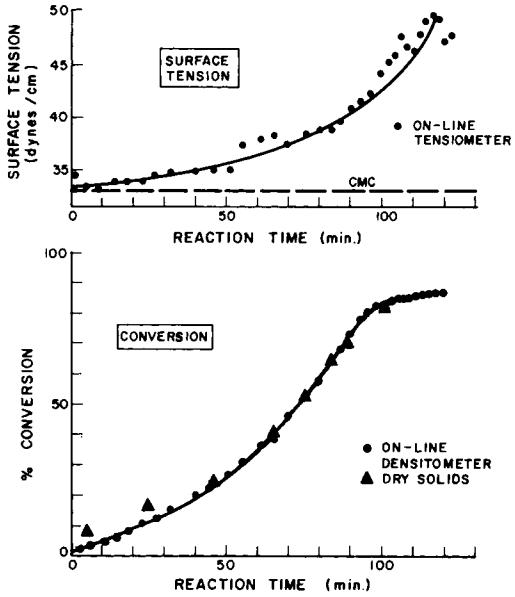

Fig. 16. Batch polymerization, [S] = 0.02 mole/L water; [I] = 0.01 mole/L water.

absence of micelles during most of the reaction. Thus, particle formation is only through relatively slow homogeneous nucleation, so that few particles are formed beyond the first few minutes, and the bulk of the polymerization consists of growing existing particles.

Figure 17 shows the results of a continuous polymerization in which apparently stable oscillations in monomer conversion were observed. These data were taken with the CSTR reactor configuration described above. Start-up was from an empty reactor, and the residence time was 47 min. Oscillatory behavior such as that reported by Greene[6] was found. In addition to monomer conversion, surface tension of the reactor effluent was monitored. It may be noted that the surface tension exhibits oscillations of approximately the same period as those of the conversion. This is due to the changes in the micelle concentration. Massive particle initiation, (indicated by a rise in monomer conversion) begins immediately when micelles are present. The presence of micelles is indicated when the surface tension drops to its value at the critical micelle concentration. As the conversion rises, more emulsifier is needed to stabilize the increasing particle area. As the emulsifier is adsorbed on the new particle surface, the micelles disappear and particle initiation drops to a very low value characteristic of homogeneous nucleation. This is shown by the rise in surface tension. With such a low rate of particle initiation, and particles leaving the reactor in the outlet stream, the conversion eventually begins to fall as the number of particles drops. When the free emulsifier concentration (increasing because of emulsifier in the feed) reaches the point where micelles form, the entire process begins again. The conversion oscillations lag the surface tension oscillations by approximately one residence time, since the effect of the new generation of particles on the monomer conversion is not immediate.

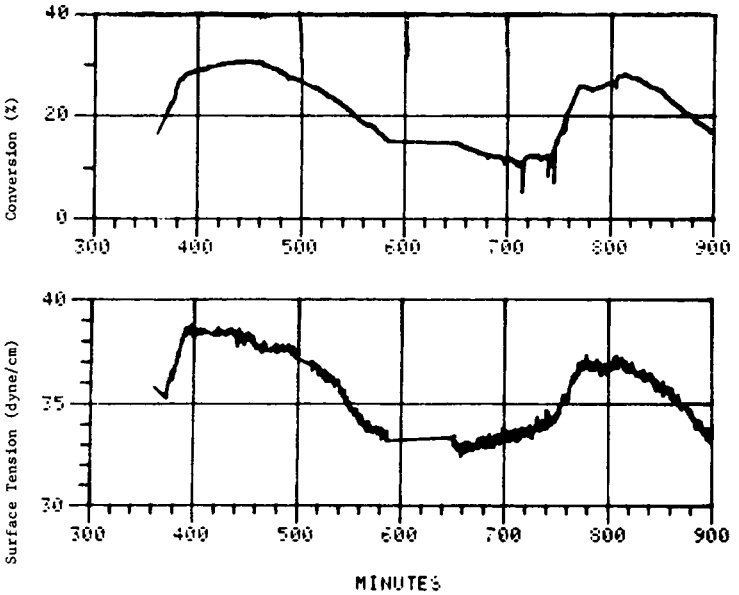

Fig. 17. Continuous polymerization, run 15, recipe 18, example of oscillatory behavior in a CSTR. Residence time = 47 min; [S] = 0.02 mole/L water; [I] = 0.01 mole/L water.

Figure 18 demonstrates the use of the bubble densitometer to monitor emulsion density during polymerization. Also shown is the emulsion density as measured by the DMA digital densitometer. As may be seen, the noise in the

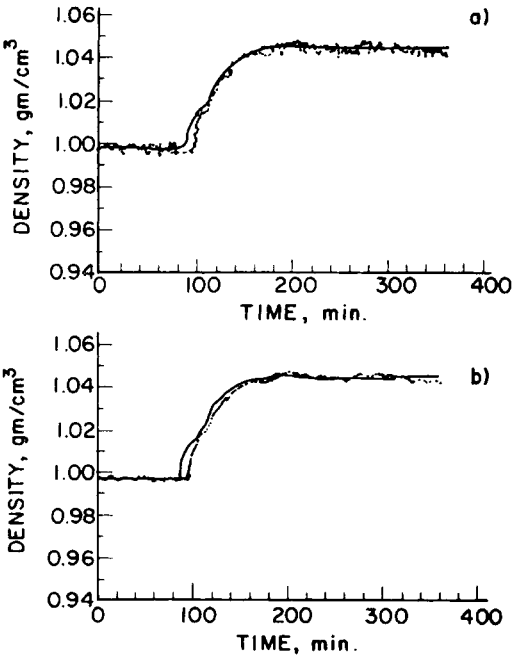

Fig. 18. Continuous polymerization, run 31, recipe 16, emulsion density by DMA (—) and bubble densitometer (- - - -). Residence time = 50 min; [S] = [I] = 0.03 mole/L water.

bubble densitometer measurement is about 0.005 to 0.01 g/cm^3. This compares favorably with the standard deviation for the calibration of 0.006 g/cm^3 (Fig. 13). Also shown in Figure 18 is the same density data filtered digitally to remove most of the noise.

Figure 19 shows the monomer conversion calculated from the filtered density data in Figure 18. The bubble densitometer was calibrated with two standards over the range 1.00 to 1.05. With this calibration and filtering, the conversion precision is even better than the ±6% suggested by Figure 13.

Based on results to date, the bubble densitometer seems promising as an on-line, approximate sensor in determining monomer conversion. Because of its simplicity and resistance to fouling, it may be valuable for monitoring polymerization. Future design modifications may substantially improve the resolution of the instrument, but it must be remembered that in order to determine conversion from emulsion density, the density must be known with extreme accuracy. Accurate determination of such small pressure differences requires state-of-the-art pressure transducers. The instrument should also prove useful in determining fluid densities in other applications.

Figure 20 shows surface tension results for the polymerization in Figure 19. The surface tension has been calculated in three different ways. The solid lines indicate surface tension as is routinely calculated using a spherical bubble approximation [eq. (14)]. The dashed line indicates the surface tension employing a nonspherical bubble model [eq. (40)] with the density correction based on the DMA density measurement. The dot–dash line indicates the surface tension employing eq. (40) with the density correction based on the bubble densitometer measurement. This last line simulates the operation of a three-orifice density-correcting bubble tensiometer as discussed previously. As may be seen, there is no discernible difference between the two density corrected measurements, indicating that highly accurate measurement of density is not necessary as a correction to surface tension. The density-corrected surface tension is consistently lower than the uncorrected by about 1 dyn/cm. This is due to the

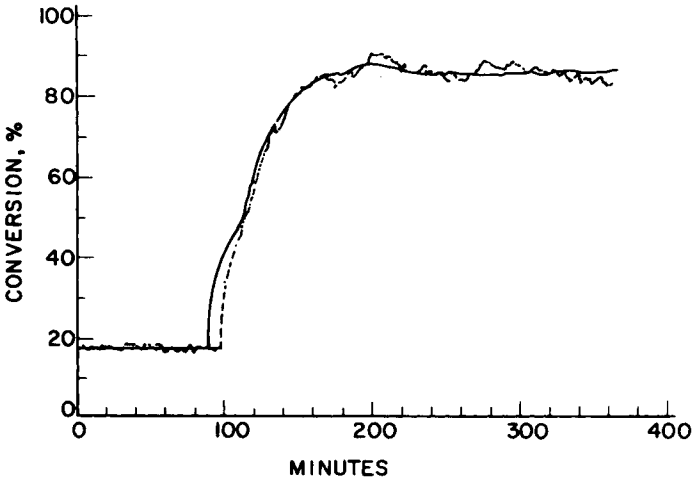

Fig. 19. Continuous polymerization, run 31, recipe 16, conversion by DMA (—) and bubble densitometer (- - -). Residence time = 50 min; [S] = [I] = 0.03 mole/L water.

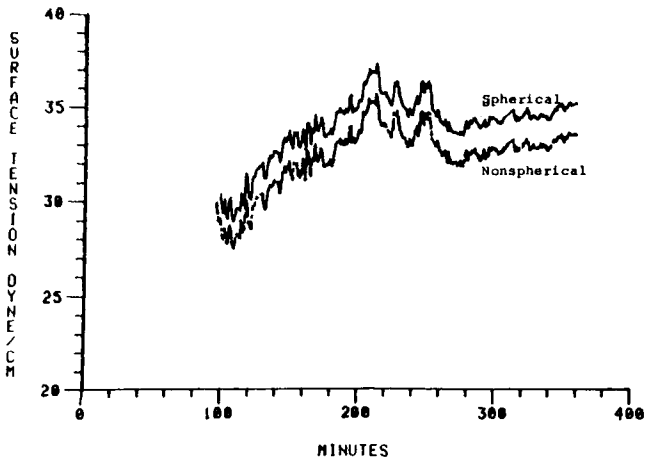

Fig. 20. Continuous polymerization, density-corrected surface tension. Residence time = 50 min; [S] = [I] = 0.03 mole/L water. (—) Spherical bubble model; (- - -) nonspherical bubble model density correction by DMA; (– • – •) nonspherical bubble model density correction by bubble densitometer. (Last two superimposed.)

fact that the emulsion density is approximately 1.05 g/cm^3. For low values of density, the corrected surface tension is higher than the uncorrected. The difference in measured surface tensions is approximately constant since the change in density on polymerization was rather small for the run shown. In systems having radically varying densities, the density correction will be for more important than in the current application.

SUMMARY

Methods have been developed for the on-line determination of surface tension and density, and the utility of the methods in monitoring batch and continuous emulsion polymerization has been demonstrated. It is expected that these techniques may have applications in the monitoring and control of a wide range of other process systems. It may be possible to monitor ethanol production during fermentation by continuously measuring density or surface tension (since the presence of ethanol significantly changes the surface tension and density of the fermentation liquor). The densitometer can be used to monitor the extent of reaction in any system in which there is a density change on reaction. The bubble tensiometer may find use in particle size and conversion control in emulsion polymerization as well as in any number of reaction or blending processes involving surface active materials. The instrument may be especially useful for control of free emulsifier concentration during continuous emulsion polymerization. In cases where it is important to measure the free emulsifier concentration above the CMC, back titration using the tensiometer is recommended. Such control of free emulsifier concentration would eliminate the intermittent particle formation phenomenon which leads to oscillatory behavior.

The prototype bubble tensiometer used in this laboratory is capable of mon-

itoring continuously a process stream with rapid response to surface tension changes, and accuracy within 1–2%. Accuracy of better than 0.5% may be possible on future units, particularly if an automatic density correction is employed. It is, however, important that the bubbling rate be sufficiently low for surface active materials so that a quasi-equilibrium is established between the bubble interface and the bulk liquid. With test fluids of low viscosity, the effect of viscosity on surface tension measurement appears to be insignificant. Tests with high viscosity materials, however, have not yet been done.

Initial investigations indicate that a commercial unit based on this design would be capable of data acquisition, alarm monitoring, and/or closed-loop control of a process variable in a laboratory, pilot plant, or production scale installation.

The authors are indebted to the National Science Foundation and the Mobil Foundation for research support and to the Rohm & Haas Co. for contributing the MMA monomer.

NOMENCLATURE

b	radius of curvature, cm
E	constant, dyn/cm
g	acceleration due to gravity, 980.7 cm/s^2
G	constant, dyn/cm
h	capillary rise, cm
k	constant, g/cm^3-s^2
l	immersion depth, cm
p	$P - \rho gl$, dyn/cm^2
P	total pressure, dyn/cm^2
Q	gas flow rate, cm^3/s
r	radius, cm
R_1, R_2	principle radii of curvature
t	time, s
V	volume, cm^3
x	conversion
z	bubble height, cm

Greek Symbols

ΔP	differential pressure, dyn/cm^2
ΔP_f	filtered differential pressure, dyn/cm^2
γ	surface tension, dyn/cm
ζ	constant, dimensionless
η	constant, dimensionless
θ	contact angle, degrees
ϕ	phase lag, s
ρ	density, g/cm^3
τ	filter time constant, s
τ_1	time constant for first order rise, dimensionless
Υ	period of bubble formation, s
ψ	$(1 + \tau_1 + \tau_1 e^{-1/\tau_1})$, dimensionless

Subscripts

ave	average
int	internal
max	maximum
0	initial

References

1. F. J. Schork and W. H. Ray, in *Emulsion Polymers and Emulsion Polymerization*, D. Bassett and A. Hamielec, Eds., American Chemical Society, New York, 1981.
2. A. W. Adamson, *Physical Chemistry of Surfaces*, Wiley, New York, 1960.
3. F. J. Schork, Ph.D. Thesis, University of Wisconsin, 1981.
4. F. Bashforth and J. C. Adams, *The Theories of Capillary Action*, University Press, Cambridge, England 1883.
5. S. Sugden, *J. Chem. Soc. London*, **121,** 858 (1922); **123,** 27 (1924).
6. R. K. Greene, R. A. Gonzalez, and G. W. Poehlein, in *Emulsion Polymerization*, I. Piirma and J. Gardon, Eds., American Chemical Society, New York, 1976.

Received September 17, 1981
Accepted November 10, 1981
Revised corrected proofs received November 4, 1982